Chemical Physics Impact 10 (2025) 100890

Contents lists available at ScienceDirect

Chemical Physics Impact

journal homepage: www.sciencedirect.com/journal/chemical-physics-impact

Full Length Article

Dielectric-tuned photon-photon coupling in a planar hybrid system

Rakesh Kumar Nayak, Meghana Mishra, Kuldeep Kumar Shrivastava, Biswanath Bhoi, Rajeev Singh *

Department of Physics, Indian Institute of Technology (Banaras Hindu University), Varanasi - 221005, India

ARTICLE INFO

Keywords:
Split ring resonator
Quantum hybrid system
Coupling Strength

ABSTRACT

This study presents photon-photon coupling (PPC) in a microwave hybrid system consisting of a Split Ring Resonator (SRR) and a Complementary Split Ring Resonator (CSRR), both acting as photon modes. Numerical simulations using CST Microwave Studio were performed to design the system and analyze the anticrossing phenomenon between the photon modes (SRR and CSRR) by examining the $|S_{21}|$ versus frequency spectra while varying the size of the CSRR. Additionally, we provide a theoretical framework to explain the observed anti-crossing phenomenon due to photon-photon interaction, which shows strong agreement with the simulation. Furthermore, we explore the influence of the substrate's dielectric constant (ε_r) on the PPC by estimating the coupling constant for different ε_r values. The results indicate that the coupling strength decreases as ε_r increases, highlighting a tunable parameter for controlling photon interactions in hybrid microwave systems. This discovery opens new avenues for developing and optimizing tunable systems, which are crucial for progress in quantum technologies.

Introduction

The modern scientific and technological landscape is largely governed by wave phenomena, which are central to both physics and engineering. Recent decades have seen a surge in research dedicated to the control and manipulation of electromagnetic waves, resulting in the observation of numerous intriguing phenomena. Within this paradigm, the advancements in quantum information science spotlight the pivotal interaction between light and matter underscoring the importance of maintaining coherence during information transfer [1,2]. The regulation and synergy of these elements hold significant promise for optimizing applications across quantum cavities for technological applications, quantum phase materials, oscillators, filters, sensors, waveguides, switches and a wide range of quantum technologies [3,4].

Among the primary observable effects of coherent light-matter interaction are vacuum Rabi splitting, Electromagnetically Induced Transparency (EIT), Rabi oscillations, and Autler-Townes splitting. Of these, EIT and its complementary phenomenon, Electromagnetically Induced Absorption (EIA), are fundamental quantum optical effects that serve as the theoretical and experimental basis for numerous applications leveraging quantum interference and quantum information processing [5–11]. The principle of EIT is grounded in the coherent coupling between two optical fields, which mitigates resonant absorption and creates a transparent medium or coupling zone. This foundational mechanism is significant in applications such as slow light dynamics, advanced optical signal modulation, quantum switching mechanisms, nonlinear wave mixing, and quantum information processing. In contrast to EIT, EIA originates from dissipative dynamics that promote light absorption within the coupling region, paving the way for applications like fast light propagation, narrowband filter implementation, absorption-switching techniques, and optical modulation technologies [12,13]. Both EIT and EIA, rooted in non-linear system dynamics, have recently been found to have analogs in a variety of systems, including photonic crystals and plasmas.

In this context, coupling-induced absorption (CIA), the linear analogue of EIA, is gaining interest due to its association with dissipative coupling, where energy dissipation becomes prominent at particular frequencies. Similarly, in the linear regime, coupling-induced transparency (CIT) serves as an analogue to EIT [10], arising from the phase relationship among system modes and enabling coherent energy transfer between interacting subsystems [10]. This phenomenon, observed through mode splitting (level repulsion, LR) and merging (level attraction, LA) near the coupling center, often requires highly demanding experimental conditions, such as ultra-low temperatures and intricate three-dimensional structures, thereby limiting its broader applicability [14–17]. As a result, significant efforts are underway to develop

* Corresponding author.
E-mail address: rajeevs.phy@iitbhu.ac.in (R. Singh).

https://doi.org/10.1016/j.chphi.2025.100890
Received 31 March 2025; Received in revised form 20 May 2025; Accepted 20 May 2025
Available online 26 May 2025

compact, planar quantum devices capable of hosting and controlling CIT and CIA phenomena. These phenomena, rooted in quantum interference, offer powerful tools for dynamically tuning light-matter interactions [15,17].

In this regard, several hybrid system configurations, such as photon-photon [18], magnon-photon [19,20], and magnon-polariton [21], have been put forward. Within these, Photon-Photon coupling (PPC) based systems have stood out, drawing considerable scientific interest, due to their exceptional tunability, which is crucial for exploring CIA by controlling the coupling strength of level attraction (LA), supported by both experimental investigations and theoretical modeling. However, limited attention has been directed toward manipulating the coupling strength through modifications in configurations of system and its components properties. In this paper, we present a PPC-based planar hybrid system composed of Split Ring Resonator (SRR) and Complementary Split Ring Resonator (CSRR) to investigate variations in the coupling strength of LA. Our study aims to control the coupling strength and adjust the coupling region of PPC by altering the dielectric constant (ε_r) of the substrate. We have also formulated a theoretical framework based on quantum mechanical modeling to understand the mechanism of PPC, which is in excellent agreement with our simulation. This work provides valuable insights into interactions in hybrid systems, offering potential pathways for future developments in quantum information processing [22].

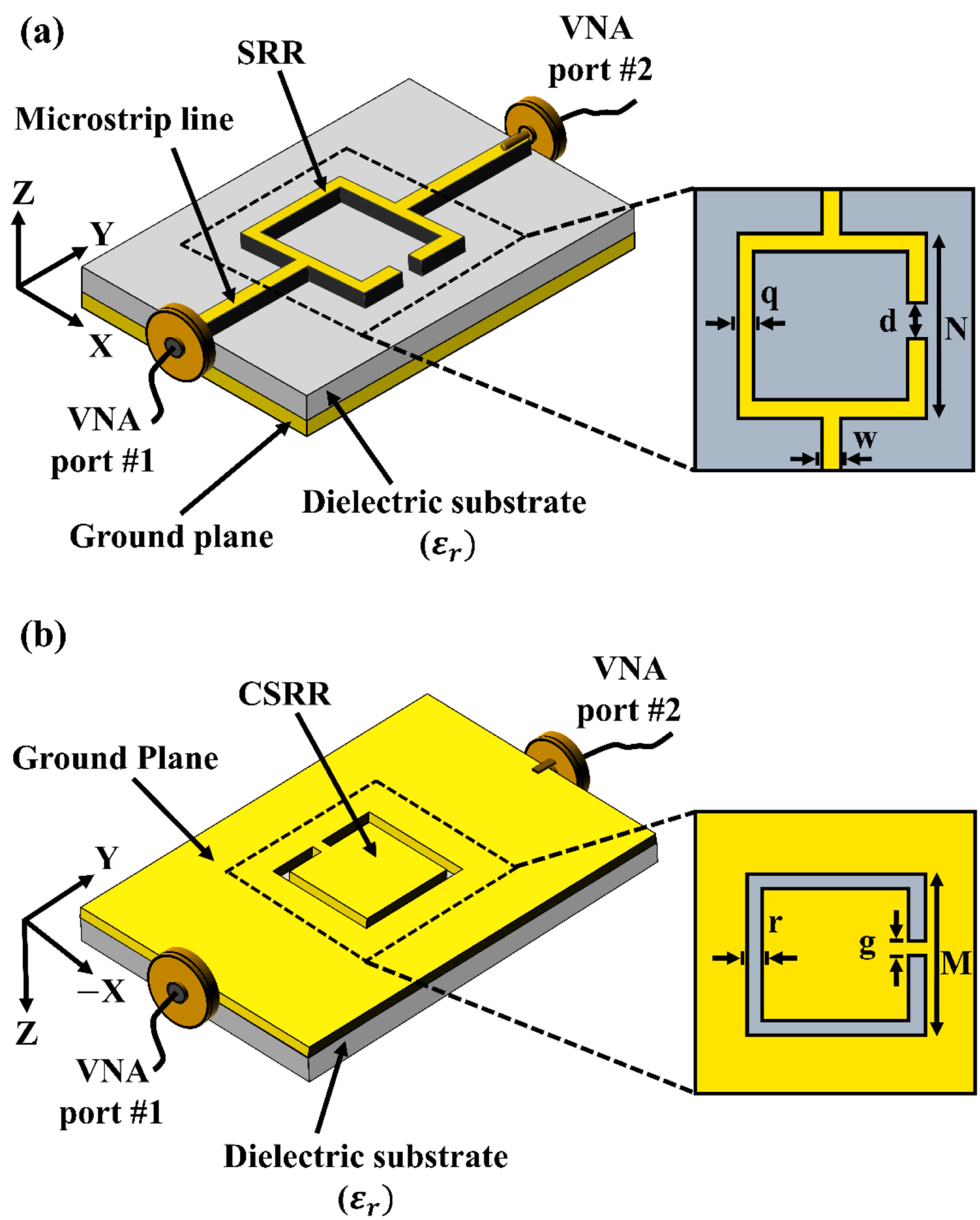

Fig. 1. The simulation framework designed to investigate the excitation of photon modes employs a planar geometry incorporating a Split-Ring Resonator (SRR) and a Complementary Split-Ring Resonator (CSRR) structure, both of which are coupled to a microstrip feeding line. In this setup, ports 1 and 2 of the feeding line are connected to a Vector Network Analyzer (VNA) to facilitate the analysis. All components are fabricated on a dielectric substrate. A schematic representation of the simulation setup for photon-photon coupling (PPC) is provided, depicting (a) the front side and (b) the back side of the structure.

Simulation set-up

In this study, CST Microwave Studio is employed to investigate the interaction between two-photon modes within a hybrid planar system comprising three layers. The top layer of this system consists of a 40 mm long microstrip line, accompanied by an SRR with dimensions $N = 8$ mm, $q = 1$ mm and $d = 0.4$ mm (see. Fig. 1(a)), while the bottom layer consists of a copper ground plane incorporating a CSRR with dimensions $g = 1$ mm, $r = 0.4$ mm and M values varies from 5 mm to 7 mm. (see Fig. 1(b)). Sandwiched between these layers, the intermediate substrate is a dielectric material with dimensions 40 mm × 30 mm × 1 mm. The SRR, microstrip line, and CSRR are all made of copper with a thickness of 0.035 mm.

Initially, the simulations were conducted for individual SRR and CSRR separately to obtain the transmission spectra $|S_{21}|$ as a function of frequency of the microwave signal in the microstrip line. The photon modes in both resonators were excited by the electromagnetic fields generated by the propagating microwave signal in the microstrip line. This microwave current, with the electric field (E) oriented vertically and the magnetic field (H) forming loops around the microstrip line. The magnetic field component of microwave current, is perpendicular to the SRR plane, induces circulating currents within the metallic rings. This results in an LC resonance excitation in SRR. Conversely, the CSRR on the bottom layer is excited by the electric field component that penetrates the substrate, interacting with the etched slots. This simulation revealed a resonance frequency peak of the SRR at 6.094 GHz and the peaks of CSRR range from 3.475 GHz to 9.712 GHz (See supplementary Fig. S1). The intrinsic damping (α) of the SRR has been evaluated based on the expression$\alpha = \Delta\omega_{\mathrm{FWHM}}/2\omega_s$. Likewise, the intrinsic damping of the CSRR was calculated as $\beta = \Delta\omega_{\mathrm{FWHM}}/2\omega_c$. Since, the values of α and β varies with different dimensions and different dielectric constants in order of 10^{-3}, these fluctuations have an insignificant effect on the fitting accuracy. Hence, we employed their average values for consistency in the calculations. The resulting average values are $\alpha = 5.517 \times 10^{-2}$ and $\beta = 5.10 \times 10^{-2}$.

To investigate photon-photon coupling between the SRR and CSRR modes, both resonators were simultaneously excited using a microwave signal propagating through the microstrip line. The SRR and CSRR are coupled via the substrate and the fields generated by the microstrip line. The SRR modifies the magnetic response, while the CSRR modifies the electric response. To observe the behavior of coupling strength between SRR and CSRR with a variation of the dielectric constant of the substrate, we have performed simulation for different dielectric constant substrates ($\mathcal{E}_r$). To ensure a characteristic impedance of 50 Ω, the width (w) of the microstrip line varies depending on the dielectric constant of the substrate. For dielectric constant $\mathcal{E}_r$ = 2.5, 3, 4, 5, 6, 7, 8, and 9, the corresponding widths of the microstrip line are taken as w = 2.78 mm, 2.45 mm, 2 mm, 1.68 mm, 1.44 mm, 1.25 mm, 1.10 mm, 0.98 mm respectively. The simulation for transmission spectra for different $\mathcal{E}_r$ value is performed by parameter sweeping of the size of CSRR from $M =$ 5 mm to 7 mm while keeping the other CSRR dimensions fixed and also the dimensions of SRR are kept fixed.

Result and discussions

Observation of anti-crossing

Fig. 2(a) presents the transmission spectra $|S_{21}|$ of the SRR-CSRR hybrid system as a function of microwave frequency for different values of M (the size of the CSRR), while keeping the SRR dimensions fixed. The spectra exhibit two distinct resonance peaks, the peak, marked by a black arrow, exhibits a relatively lower gain and shows a strong dependence on 'M' the size of the CSRR. As M increases $M = 5$ to 7 mm, this peak gradually shifts to lower frequencies and eventually intersects with the higher gain resonance peak indicated by a red arrow.

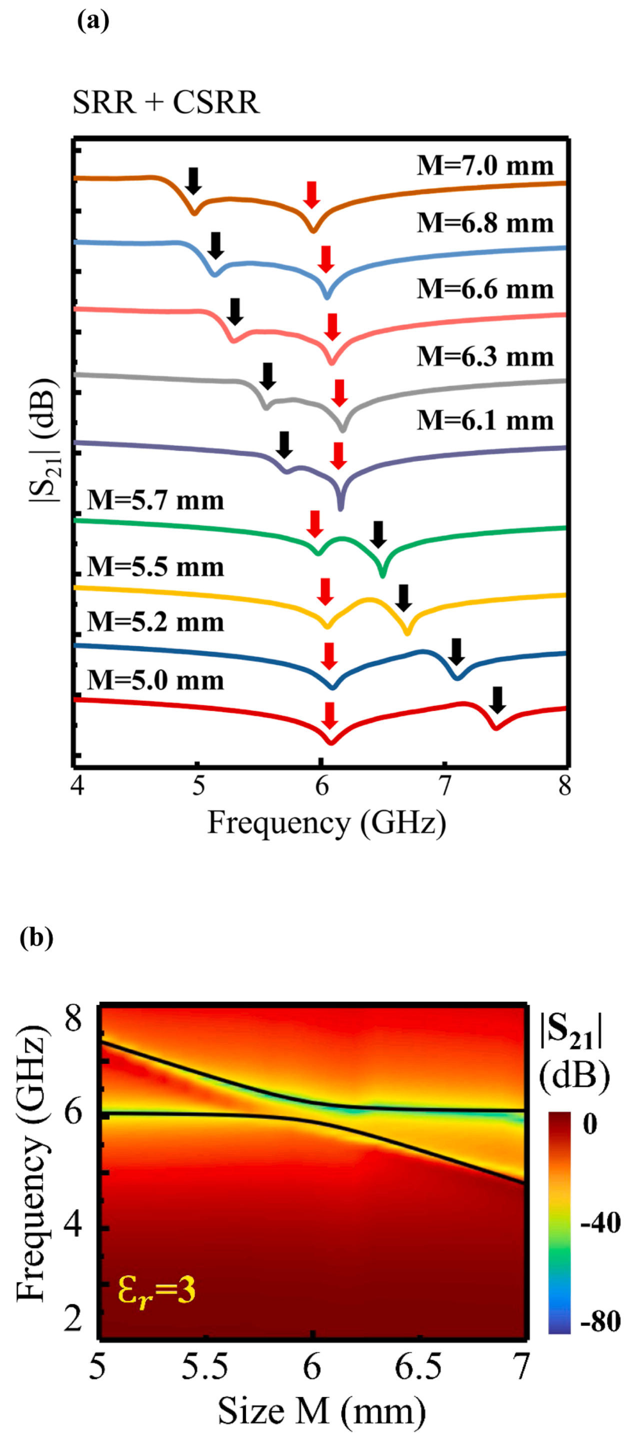

Fig. 2. (a) The stacked plot of the transmission spectra $|S_{21}|$ is shown as a function of microwave frequency for multiple sizes of the CSRR (M). This analysis captures the dynamic response of the planar hybrid system that integrates both the SRR and CSRR, thereby revealing the interaction mechanism between two photon modes. (b) The transmission spectra of the SRR-CSRR hybrid system are depicted using a colormap, which visualizes the frequency-dependent response of the structure. The overlaid solid line represents the theoretical model fitting, demonstrating consistency between the numerical simulations and analytical predictions for a dielectric substrate with a dielectric constant of $\varepsilon_r = 3$.

The resonance peak, indicated by a red arrow remains largely unaffected by changes in the CSRR dimension, suggesting its association with a stable photon mode. This behavior of peak marked by black arrow aligns with simulations conducted exclusively for the CSRR (see Supplementary Fig. S2), which demonstrate that its resonance frequency decreases as M increases. This frequency shift results from an increase in the effective inductance of the CSRR, thereby lowering the resonance frequency in accordance with the relation $\omega_c = 1/\sqrt{L_c C_c}$. Therefore, During PPC between the CSRR and SRR modes, the resonance peak marked by black arrow that continuously shifts toward lower frequencies is identified as the CSRR photon mode, while the fixed resonance peak corresponds to the SRR photon mode. Notably, as the CSRR resonance approaches that of the SRR, the amplitude of its peak increases, whereas the amplitude of the SRR peak decreases. Once the peaks move apart, their original amplitudes are restored. This reciprocal modulation of peak intensities signifies coherent energy exchange between the two coupled resonators. As a result of this interaction, two distinct hybrid modes emerge, each representing a superposition of the original SRR and CSRR resonances, as clearly illustrated in the colormap of Fig. 2(b). These hybrid modes exhibit a characteristic frequency splitting: one

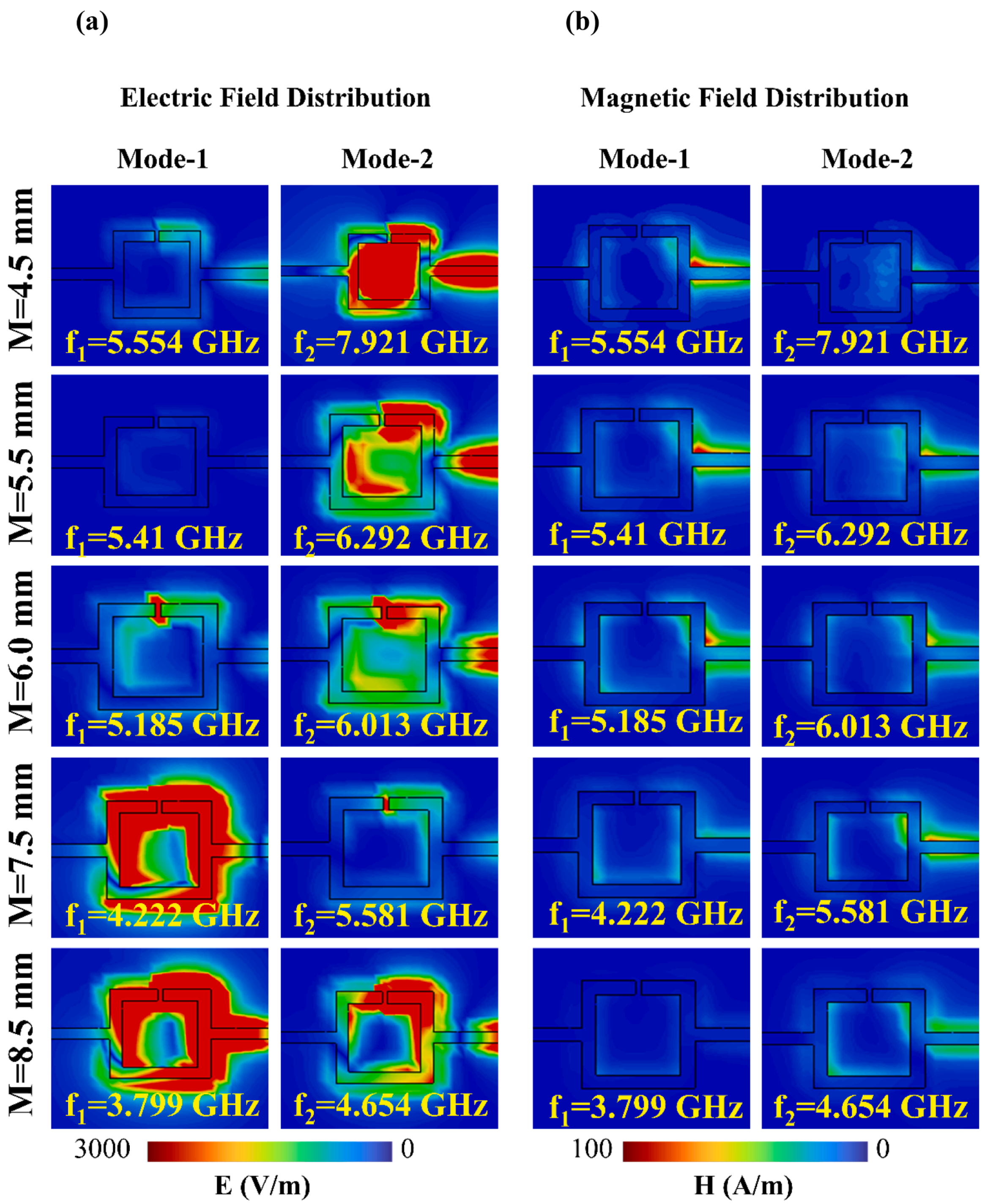

Fig. 3. Simulation result of (a) electric field distribution (b) magnetic field distribution for a planar hybrid system integrating a SRR and CSRR with different sizes of CSRR ($M = 4.5$ mm, 5.5 mm, 6.0 mm, 7.5 mm, 8.5 mm). The left panel represents mode-1 and the right panel corresponds to mode-2. The color gradient represents the field intensity, with red denoting the highest field concentration and blue indicating low-field regions.

branch shifts to a higher frequency and the other to a lower frequency, relative to the point at which the uncoupled modes would have intersected. This splitting directly reflects the coupling strength and serves as a clear spectral signature of strong coupling and level repulsion. This distinct anti-crossing effect provides direct evidence of the coupling between the two photon modes [23].

The coupling mechanism is further illustrated in Fig. 3(a) and (b), which present the electric and magnetic field distributions due to PPC. In Fig. 3(a), as *M* increases, the electric field strength of mode-1 decreases, while for mode-2, it increases correspondingly. Similarly, in Fig. 3(b), the magnetic field strength of mode-1 diminishes with increasing *M* whereas mode-2 exhibits enhanced magnetic field strength. This redistribution of field intensity underscores the interaction between the coupled photon modes and provides insights into the energy transfer dynamics within the hybrid resonator system.

Analytical model

A quantum theoretical framework is discussed to describe the coupling dynamics between the SRR and CSRR, allowing for an estimation of the coupling strength. The schematic representation of this model is shown in Fig. 4.

The general Hamiltonian for SRR, CSRR and microstrip line, after applying the rotating wave approximation is given by [4,24–27],

$$H = \hbar(\omega_s - i\alpha)\hat{s}^\dagger\hat{s} + \hbar(\omega_c - i\beta)\hat{c}^\dagger\hat{c} + \hbar\Upsilon(\hat{s}\hat{c}^\dagger + \hat{s}^\dagger\hat{c}) + \hbar\int\omega_k\hat{p}_k^\dagger\hat{p}_k dk + \hbar\int\nu_s(\hat{s}\hat{p}_k^\dagger + \hat{s}^\dagger\hat{p}_k)dk + \hbar\int v_c(\hat{c}\hat{p}_k^\dagger + \hat{c}^\dagger\hat{p}_k)dk \quad (1)$$

Where, the operators $\hat{s}$ and $\hat{s}^\dagger$ are the annihilation and creation operators of the SRR mode, while $\hat{c}$ and $\hat{c}^\dagger$ are the annihilation and creation operators of the CSRR mode. The parameters ω_s and ω_c correspond to the resonance frequencies of the SRR and CSRR, respectively, in the absence of coupling. Additionally, α and β characterize the intrinsic damping rates associated with the SRR and CSRR, respectively. The coupling strength is expressed as $\Upsilon = J + i\Gamma$, where J and Γ denote the real-valued components associated with the coherent and dissipative interactions between the SRR and CSRR, respectively. In this Hamiltonian description, an additional coupling is introduced via traveling photons propagating along the microstrip line, with their influence being integrated over the full real domain, extending indefinitely in both directions. Due to their bosonic nature, these photons are described by the creation and annihilation operators $\hat{p}_k^\dagger$ and $\hat{p}_k$ respectively, which satisfy the commutation relation $[\hat{p}_k, \hat{p}_{k'}^\dagger] = \delta(k - k')$. Here, k denotes the wave vector, while ω_k in Eq. (1) represents the frequency associated with the traveling photons. The interaction between the traveling photons propagating along the microstrip line and the individual modes (SRR or CSRR), is captured in the final term of the Hamiltonian, where the interaction strengths, denoted by ν_s and v_c, are modeled as linear functions of $\hat{p}_k^\dagger$ and $\hat{p}_k$.

Now, the equations of motion of the operators $\hat{s}$ and $\hat{c}$ are given by

$$\dot{\hat{s}} = \frac{-i}{\hbar}[\hat{s}, H] = -i\widetilde{\omega}_s\hat{s} - \int i\nu_s\hat{p}_k dk - i\Upsilon\hat{c} \quad (2)$$

$$\dot{\hat{c}} = \frac{-i}{\hbar}[\hat{c}, H] = -i\widetilde{\omega}_c\hat{s} - \int i\nu_c\hat{p}_k dk - i\Upsilon\hat{s} \quad (3)$$

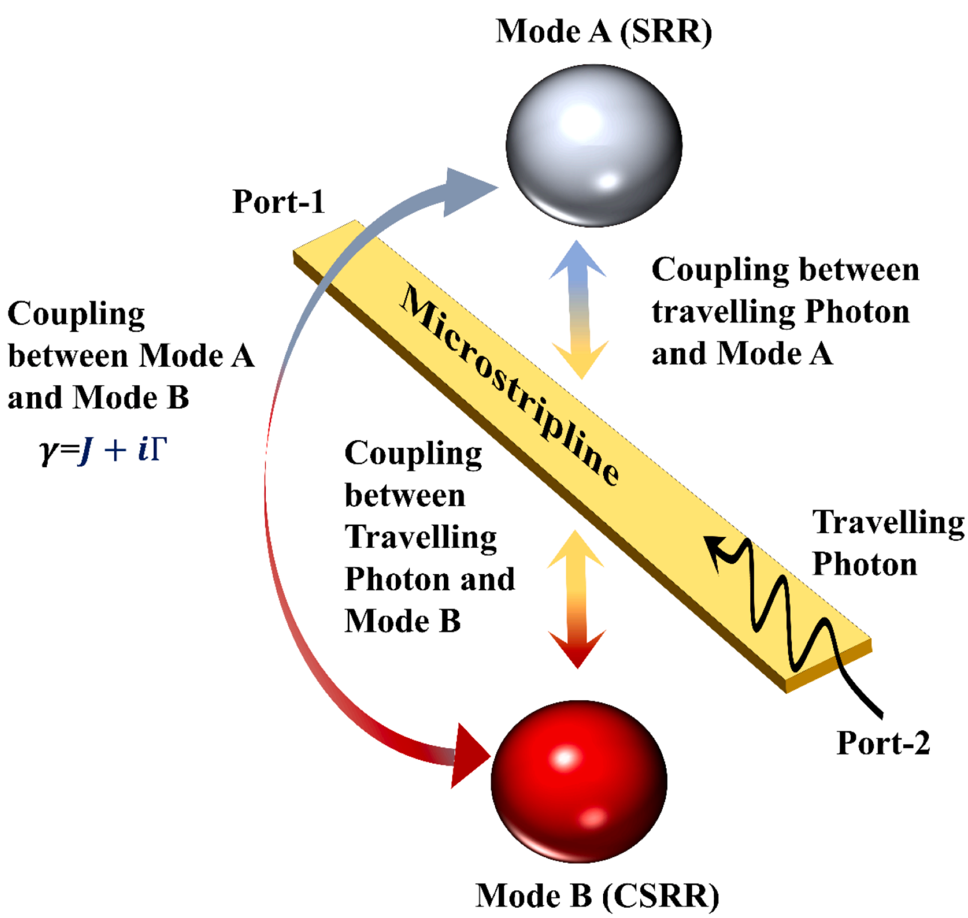

Fig. 4. Schematic representation of the quantum model illustrating the interaction among the microstrip line, SRR, and CSRR. The diagram highlights two distinct modes, A and B, which share a common signal line while exhibiting different system attributes. A traveling photon is coupled with both Mode A and Mode B, facilitating a coupling between these two modes and enabling their interaction through the common signal pathway.

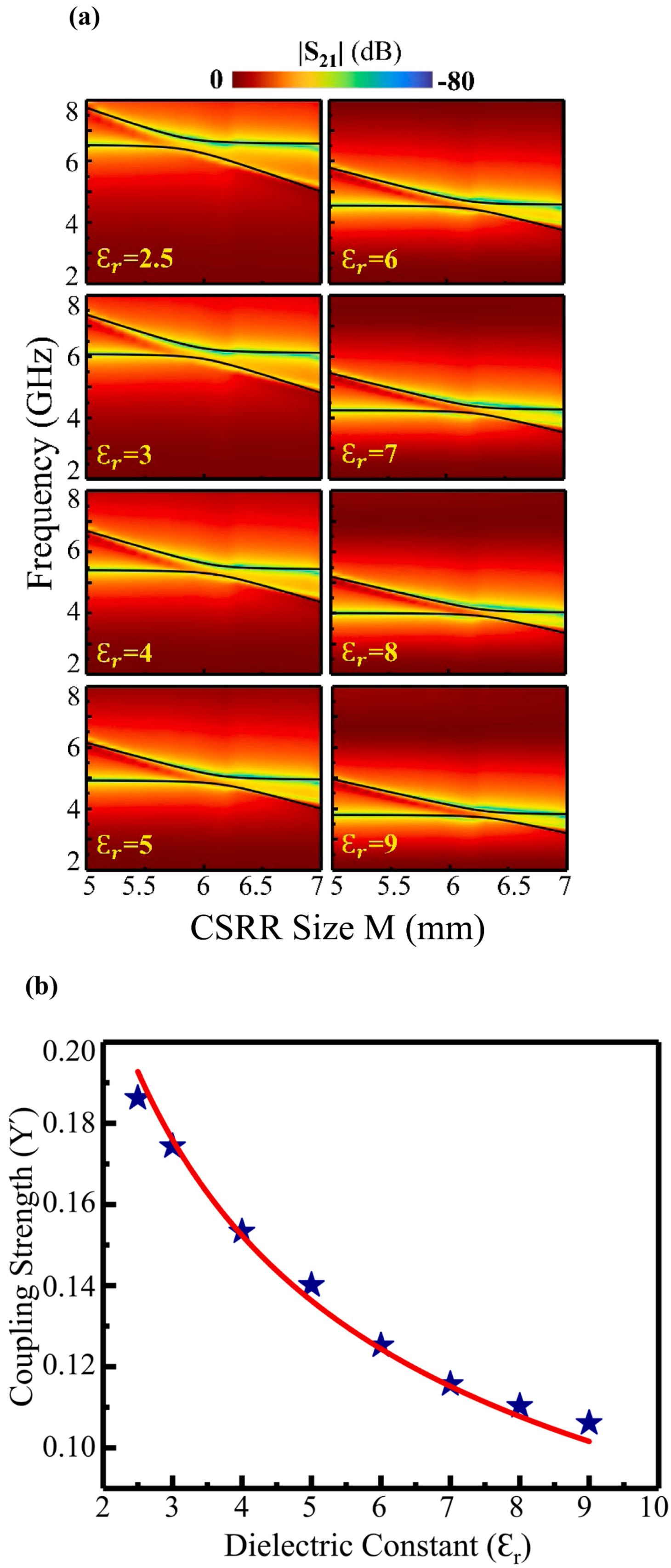

(caption on next page)

Fig. 5. (a) Colormap of the transmission spectra for the SRR-CSRR hybrid system, with the dielectric constant varied from 2.5 to 9. The color scale represents the transmission intensity, revealing the change in mode interaction with increasing dielectric constant. The solid lines indicate the theoretical eigenvalues, with upper and lower curve fits corresponding to the respective transmission plots. (b) This plot illustrates the relationship between coupling strength (Υ′)and the dielectric constant (ε_r). The solid red line represents the fitted data, providing a smooth trend, while the blue star markers indicate the values of Υ′ as a function of ε_r calculated from theoretical quantum model. The comparison between the fitted curve and the computed data points highlights the consistency of the model in capturing the dependence of coupling strength on the dielectric properties of the system.

Where $\widetilde{\omega}_s = (\omega_s - i\alpha)$ and $\widetilde{\omega}_c = (\omega_c - i\beta)$ represent the complex resonance frequencies of the SRR and CSRR, respectively. By incorporating the solution of the traveling photon mode into the above equation, the extrinsic damping rates of the SRR and CSRR are derived as $\mu = 2\pi\nu_s^2$ and $\lambda = 2\pi\nu_c^2$ respectively. The numerical values are found to be $\mu = 0.0421$ and $\lambda = 0.0578$. Furthermore, the above two equations lead to the formulation of a coupling matrix given by

$$H_{coupling} = \begin{pmatrix} \widetilde{\omega}_{s'} & \Upsilon' \\ \Upsilon' & \widetilde{\omega}_{c'} \end{pmatrix} \quad (4)$$

Where, $\widetilde{\omega}_{s'} = \omega_s - i(\alpha + \mu)$, $\widetilde{\omega}_{c'} = \omega_c - i(\beta + \lambda)$ and $\Upsilon' = J + i\Gamma'$, where substituting the value $\Gamma' = \Gamma + 2\pi\nu_s\nu_c$ gives $\Upsilon' = J + i(\Gamma' + 2\pi\nu_s\nu_c)$. where numerical value is $\Gamma' = 0.052$. The complex eigen frequencies $\omega_\pm$ of the coupling matrices are given by

$$\omega_\pm = \frac{\widetilde{\omega}_{s'} + \widetilde{\omega}_{c'} \pm \sqrt{(\widetilde{\omega}_{s'} - \widetilde{\omega}_{c'})^2 + 4(\Upsilon')^2}}{2} \quad (5)$$

We have numerically determined $\omega_\pm = \omega_{real} + i\omega_{imag}$ using this Eq. (5) and achieved a good agreement between the fitted real part of the eigenvalues (ω_{real}) and the simulation dispersion as illustrated by the solid black line with the upper branch indicating the higher-frequency hybrid mode (ω_+) and the lower branch corresponding to the lower-frequency mode (ω_-) in Fig. 2(b), yielding a coupling strength value of 174.3 MHz.

Tuning of coupling strength

In order to examine the variation of coupling strength between two modes with changes in the dielectric constant of the substrate, the numerical CST microwave simulations were performed for different dielectric constant $\varepsilon_r = 2.5, 3, 4, 5, 6, 7, 8, 9$ and plotted corresponding dispersion spectra respectively, shown in Fig. 5(a). Additionally, numerical fitting was applied to the transmission spectra using Eq. (5), with the fitted results represented by the solid black line in Fig. 5(a). The transmission spectra $|S_{21}|$, from Fig. 5(a), reveal a maximum coupling strength of 186.2 MHz for $\varepsilon_r = 2.5$, which gradually decreases with increasing ε_r, reaching a minimum coupling strength of 106.1 MHz for $\varepsilon_r = 9$.

The variation of coupling strength corresponding to ε_r are shown in Fig. 5(b). Here, we noticed that Υ′ decreases as ε_r increases. This result signifies that as ε_r increases, the propagation of electromagnetic waves through the material slows down. This reduction in phase velocity results in an increased ability of the substrate to store electric energy, leading to a higher concentration of the electric field within the substrate. Consequently, the electric field becomes more confined within the dielectric layer, thereby reducing the extent of field interaction between the SRR on the top layer and the CSRR on the bottom layer. Since Υ′ between these resonators is dependent on the overlap of their electromagnetic fields, its magnitude diminishes as ε_r increases. This behavior can be mathematically described through complex eigen frequencies analysis. From Eq. (5) frequency gap $(\omega_+ - \omega_-)$ can be written as

$$(\omega_+ - \omega_-) = \sqrt{(\widetilde{\omega}_{s'} - \widetilde{\omega}_{c'})^2 + 4(\Upsilon')^2} \quad (6)$$

Now on putting the value of parameters $\widetilde{\omega}_{s'}$, $\widetilde{\omega}_{c'}$ and Υ′ in Eq.(6), we get the $(\omega_+ - \omega_-)$ in real and imaginary parts [26]. Since in level repulsion, the imaginary part of $(\omega_+ - \omega_-)$ vanishes at anticrossing centre so equating it to zero, which gives (see supplementary S3),

$$J = \frac{[(\alpha + \mu) - (\beta + \lambda)](\omega_s - \omega_c)}{4\Gamma'} \quad (7)$$

Since the parameters α, β, λ, Γ′ remain fixed during the theoretical fitting, so the coherent coupling strength (J) is directly proportional to $(\omega_s - \omega_c)$. The resonance frequency of a resonator is given by $\frac{1}{\sqrt{LC}}$, it will be directly proportional to $\frac{1}{\sqrt{\varepsilon_r}}$, considering that the capacitance is expressed as $C = \varepsilon_r A/h$. Therefore, the frequency difference $(\omega_s - \omega_c)$ exhibits the same inverse square root dependence on ε_r, leading to a similar dependence for J. Since the level repulsion phenomenon satisfies the condition, $J >> \Gamma'$, furthermore Υ′=J+i Γ′, with magnitude primarily depends on J and thus Υ′ follows the same inverse square root dependency on ε_r,

$$\Upsilon' = \frac{\Upsilon_0}{\sqrt{\varepsilon_r}} \quad (8)$$

The dependence of Υ′on ε_r, is illustrated in Fig. 5(b), where the Υ′ values were derived from an eigenvalue fit to the simulation results for the corresponding ε_r which show excellent agreement with Eq. (8) and yield Υ_0= 0.3047 GHz.

In Fig. 5(a), we notice that the frequencies of each mode with the anticrossing center are also shifting towards a lower frequency region with an increase of ε_r. This shift arises because, upon applying a microwave to the microstrip line, the electromagnetic wave propagates partly in the substrate (ε_r) and partly in the air (ε_0=1). As a result, the effective permittivity lies between these two values and depends on the geometry and the relative distribution of the fields. Since the resonant frequency of SRR and CSRR is given by $\omega = \frac{1}{\sqrt{LC}}$, which primarily depending on the inductance and capacitance of its geometry, so it directly affects the resonant frequency of SRR and CSRR. Thus, increasing the dielectric constant of the substrate reduces the resonant frequency of both SRR and CSRR, resulting in the anticrossing shift toward lower frequencies. Overall, our finding indicates that tuning the dielectric constant of the substrate plays a crucial role in modifying both the coupling strength and coupling region. To achieve strong PPC between two modes, the substrate of hybrid system should be made of lower dielectric constant. This finding has important implications for the advancement of high-sensitivity sensing devices and quantum information processing, where controlled coupling mechanisms are crucial for enhancing device functionality and performance.

Summary

A planar microwave hybrid system, incorporating a split-ring resonator and a complementary split-ring resonator, was meticulously designed to facilitate photon-photon coupling. To investigate the coupling behavior, dispersion spectra were simulated while systematically varying the dielectric constant of the substrate, maintaining a constant thickness throughout the study. The results revealed a pronounced reduction in coupling strength with an increase in the dielectric constant, highlighting the critical role of the dielectric properties of the substrate in governing the interaction dynamics. To further substantiate these findings, a quantum analytical model was developed, which exhibited strong agreement with the simulation data, validating the theoretical framework underlying the observed coupling phenomena. This comprehensive approach not only enhances the understanding of photon-photon interactions but also enables precise tuning of the anti-crossing region to achieve strong coupling. These advancements are instrumental in controlling light-matter interactions, with significant implications for quantum information technology, fostering the development of highly efficient microwave photonic devices and metamaterials with tailored electromagnetic properties.

Statements & declarations

Funding: The authors declare that grants were received from CSTUP and SERB during the preparation of this manuscript.

CRediT authorship contribution statement

Rakesh Kumar Nayak: Writing – original draft, Visualization, Validation, Methodology, Formal analysis, Data curation, Conceptualization. **Meghana Mishra:** Writing – review & editing, Visualization. **Kuldeep Kumar Shrivastava:** Methodology, Formal analysis. **Biswanath Bhoi:** Writing – review & editing, Visualization, Validation, Supervision, Software, Resources, Project administration, Methodology, Investigation, Funding acquisition, Conceptualization. **Rajeev Singh:** Writing – review & editing, Visualization, Validation, Supervision, Software, Resources, Project administration, Methodology, Investigation, Funding acquisition, Conceptualization.

Declaration of competing interest

The authors declare that they have no known competing financial interests or personal relationships that could have appeared to influence the work reported in this paper.

Acknowledgments

The work was supported by the Council of Science & Technology, Uttar Pradesh (CSTUP), (Project Id: 4482, CST, U.P. sanction no: CST/D-7/8, Project Id: 2470, CST, U.P. sanction no: CST/D-1520). B. Bhoi acknowledges support by the Science and Engineering Research Board (SERB) India- SRG/2023/001355. R.K. Nayak acknowledges computational facilities provided by IIT (BHU) Varanasi.

Supplementary materials

Supplementary material associated with this article can be found, in the online version, at doi:10.1016/j.chphi.2025.100890.

Data availability

Data will be made available on request.

References

[1] P.W. Shor, Polynomial-time algorithms for prime factorization and discrete logarithms on a quantum computer, SIAM J. Comput. 26 (1997) 1484–1509, https://doi.org/10.1137/s0097539795293172.

[2] M. Wallquist, K. Hammerer, P. Rabl, M. Lukin, P. Zoller, Hybrid quantum devices and quantum engineering, Phys. Scripta 2009 (2009) 014001, https://doi.org/10.1088/0031-8949/2009/T137/014001.

[3] S.-H. Wei, B. Jing, X.-Y. Zhang, J.-Y. Liao, C.-Z. Yuan, B.-Y. Fan, C. Lyu, D.-L. Zhou, Y. Wang, G.-W. Deng, H.-Z. Song, D. Oblak, G.-C. Guo, Q. Zhou, Towards real-world quantum networks: a review, Laser Photon. Rev. 16 (2022) 2100219, https://doi.org/10.1002/lpor.202100219.

[4] T. Tiwari, K.K. Shrivastava, D. Roy, R. Singh, A modified quasi-classical analysis to capture the effects of strong interaction in open QED lattices, Annalen der Physik 536 (2024) 2300402, https://doi.org/10.1002/andp.202300402.

[5] M. Fleischhauer, A. Imamoglu, J.P. Marangos, Electromagnetically induced transparency: optics in coherent media, Rev. Mod. Phys. 77 (2005) 633–673, https://doi.org/10.1103/RevModPhys.77.633.

[6] B. Cumming, A. Akulshin, A. Sidorov, R. McLean, P. Hannaford, Dynamic electromagnetically induced absorption, in: ACOFT/AOS 2006 - Australian Conference on Optical Fibre Technology/Australian Optical Society, 2006.

[7] L. Ma, O. Slattery, X. Tang, Optical quantum memory based on electromagnetically induced transparency, J. Opt. 19 (2017) 043001, https://doi.org/10.1088/2040-8986/19/4/043001.

[8] S.E. Harris, J.E. Field, A. Imamoğlu, Nonlinear optical processes using electromagnetically induced transparency, Phys. Rev. Lett. 64 (1990) 1107–1110, https://doi.org/10.1103/PhysRevLett.64.1107.

[9] Y. Yu, X. Xi, X. Sun, Observation of mechanical bound states in the continuum in an optomechanical microresonator, Light: Sci. Applic. 11 (2022) 328, https://doi.org/10.1038/s41377-022-00971-w.

[10] J.W. Rao, Y.T. Zhao, Y.S. Gui, X.L. Fan, D.S. Xue, C.M. Hu, Controlling microwaves in Non-Hermitian metamaterials, Phys. Rev. Appl. 15 (2021), https://doi.org/10.1103/PhysRevApplied.15.L021003. L021003.

[11] B. Bhoi, B. Kim, H.-C. Jeon, S.-K. Kim, Coupling-induced transparency and absorption in a magnon–multiphoton hybrid system, J. Appl. Phys. 132 (2022) 243901, https://doi.org/10.1063/5.0122360.

[12] D.V. Brazhnikov, A.M. Tumaikin, V.I. Yudin, A.V. Taichenachev, Electromagnetically induced absorption and transparency in magneto-optical resonances in an elliptically polarized field, J. Opt. Soc. Am. B 22 (2005) 57–64, https://doi.org/10.1364/JOSAB.22.000057.

[13] R. Ning, J. Bao, Z. Chen, Z. Jiao, Electromagnetically induced absorption in metamaterials and applications in the infrared range, J. Electron. Mater. 48 (2019) 4733–4739, https://doi.org/10.1007/s11664-019-07263-x.

[14] T. Zheng, P. Wang, B. Wei, B. Lu, B. Cao, F. Lei, Three-pathway electromagnetically induced transparency and absorption based on coupled superconducting resonators, Phys. Rev. A 108 (2023) 053105, https://doi.org/10.1103/PhysRevA.108.053105.

[15] N.R. Bernier, L.D. Tóth, A.K. Feofanov, T.J. Kippenberg, Level attraction in a microwave optomechanical circuit, Phys. Rev. A 98 (2018) 023841, https://doi.org/10.1103/PhysRevA.98.023841.

[16] Y. Li, V.G. Yefremenko, M. Lisovenko, C. Trevillian, T. Polakovic, T.W. Cecil, P. S. Barry, J. Pearson, R. Divan, V. Tyberkevych, C.L. Chang, U. Welp, W.-K. Kwok, V. Novosad, Coherent coupling of two remote magnonic resonators mediated by superconducting circuits, Phys. Rev. Lett. 128 (2022) 047701, https://doi.org/10.1103/PhysRevLett.128.047701.

[17] M.-W. Hu, W. Yu, Y.-P. Wang, Auxiliary mode mediated coherent and complex couplings in a cavity magnonic system, Annalen der Physik 534 (2022) 2100534, https://doi.org/10.1002/andp.202100534.

[18] H.Le Jeannic, A. Tiranov, J. Carolan, T. Ramos, Y. Wang, M.H. Appel, S. Scholz, A. D. Wieck, A. Ludwig, N. Rotenberg, L. Midolo, J.J. García-Ripoll, A.S. Sørensen, P. Lodahl, Dynamical photon–photon interaction mediated by a quantum emitter, Nat. Phys. 18 (2022) 1191–1195, https://doi.org/10.1038/s41567-022-01720-x.

[19] B. Bhoi, B. Kim, J. Kim, Y.-J. Cho, S.-K. Kim, Robust magnon-photon coupling in a planar-geometry hybrid of inverted split-ring resonator and YIG film, Sci. Rep. 7 (2017) 11930, https://doi.org/10.1038/s41598-017-12215-8.

[20] B. Bhoi, B. Kim, S.-H. Jang, J. Kim, J. Yang, Y.-J. Cho, S.-K. Kim, Abnormal anticrossing effect in photon-magnon coupling, Phys. Rev. B 99 (2019) 134426, https://doi.org/10.1103/PhysRevB.99.134426.

[21] O. Lee, K. Yamamoto, M. Umeda, C.W. Zollitsch, M. Elyasi, T. Kikkawa, E. Saitoh, G.E.W. Bauer, H. Kurebayashi, Nonlinear magnon polaritons, Phys. Rev. Lett. 130 (2023) 046703, https://doi.org/10.1103/PhysRevLett.130.046703.

[22] M. Harder, C.-M. Hu, Chapter two - cavity spintronics: an early review of recent progress in the study of magnon–photon level repulsion. Solid State Physics, Academic Press, 2018, pp. 47–121. R.E. Camley and R.L. Stamps, Editors.

[23] Y.-P. Wang, J.W. Rao, Y. Yang, P.-C. Xu, Y.S. Gui, B.M. Yao, J.Q. You, C.M. Hu, Nonreciprocity and unidirectional invisibility in cavity magnonics, Phys. Rev. Lett. 123 (2019) 127202, https://doi.org/10.1103/PhysRevLett.123.127202.

[24] J.W. Rao, Y.P. Wang, Y. Yang, T. Yu, Y.S. Gui, X.L. Fan, D.S. Xue, C.M. Hu, Interactions between a magnon mode and a cavity photon mode mediated by traveling photons, Phys. Rev. B 101 (2020) 064404, https://doi.org/10.1103/PhysRevB.101.064404.

[25] M. Harder, B.M. Yao, Y.S. Gui, C.-M. Hu, Coherent and dissipative cavity magnonics, J. Appl. Phys. 129 (2021), https://doi.org/10.1063/5.0046202.

[26] K.K. Shrivastava, A. Sahu, B. Bhoi, R. Singh, Unveiling photon–photon coupling induced transparency and absorption, J. Phys. D Appl. Phys. 57 (2024) 465305, https://doi.org/10.1088/1361-6463/ad6613.

[27] C.C. Gerry, P.L. Knight, Introductory Quantum Optics, Cambridge university press, 2023.